SUPPLEMENTARY MATERIAL

Supplementary Methods

1. Neuropsychological test battery

Patients, eligible for further examination underwent a 45-min cognitive test battery as soon as infectivity was no longer present according to the in-house guidelines of the University Hospital Freiburg. The battery consisted of six standardized neuropsychological tests, administered by a neuropsychologist or trained neurologist in a quiet and undisturbed environment and was designed to assess neuropsychological sequelae associated with widely distributed brain functions, such as memory, executive function, and attention. The tests are described in **Supplementary Table 1**. Composite scores for the individual domains were formed.

We used German versions of internationally established and published neuropsychological tests. Each test came with mean and standard deviation of an unimpaired normative sample. As standard, these normative samples do not report any neurological or psychiatric complaints. Where available, norms were stratified by age and education. Based on these available norms, the individual z-scores were calculated, as in previous studies (Lazar *et al.*, 2018). In case of the Color-Word-Interference Test ("Stroop-Test"; Bäumler, 1985) the raw scores are assigned a T-score based on the norms which were used to calculate a z-score. Since results were normally distributed, this was considered appropriate.

2. Dynamic susceptibility contrast (DSC)-Perfusion analysis

3D T1w imaging datasets were automatically segmented into white matter (WM), grey matter (GM) and cerebrospinal fluid (CSF) using an in-house post-processing platform (NORA; www.nora-imaging.org) and non-linear transformed to MNI space by using the segmentation algorithm of SPM12 (http://www.fil.ion.ucl.ac.uk/spm/software/spm12). 30 age-matched subjects without structural brain lesion served as control group (17 female and 13 male; mean age 66.8 ± 12.7 years). Perfusion imaging

was acquired with the same parameters as in patients (see main text). No pathological pattern of perfusion was observed in the standard perfusion-weighted metrics (cerebral blood flow / CBF, cerebral blood volume / CBV and time-to-max / Tmax). We used the LPBA 40 atlas (Shattuck *et al.*, 2008) to define 10 regions of interest (ROI; 5 per hemisphere), covering the frontal, temporal, parietal and occipital lobe structures as well as the cerebellum. The ROI were warped into the individual´s space and perfusion metrics were analyzed based on these ROIs. Furthermore, a voxel-based analysis of GM and WM perfusion metrics with age as a covariate was performed as a group comparison.

3. ^{18}FDG PET Imaging

After the subjects fasted for at least 6 h, 215 ± 13 MBq ^{18}FDG were intravenously injected under normoglycemic, resting conditions (eyes open and ears unplugged at ambient noise). At 50 min after injection, a 10-min PET scan was acquired, during which the position of the patient's head was gently restrained with elastic tape and carefully monitored. Using low-dose CT for attenuation correction, a fully corrected emission dataset was reconstructed with the vendor-specific, line-of-response time-of-flight ordered-subsets 3-dimensional iterative reconstruction algorithm using spherically symmetric basis functions (so-called blob ordered subset time-of-flight reconstruction; number of iterations, 5; number of subsets, 11; 2-mm Gaussian post-filtering; resulting voxel size, 1.0 x 1.0 x 1.0 mm), yielding a reconstructed, isotropic image resolution of approximately 4.5–5 mm full width at half maximum (FWHM). We did not use resolution recovery to avoid Gibbs artifacts.

4. Selection of Control Patients

Aforementioned novel fully-digital PET/CT scanner provides superior spatial resolution, allowing for quantitative imaging of small brain structures like brainstem nuclei (Speck *et al.*, 2020). However, given the recent advent of fully-digital PET in clinical routine and installation of the system in our institution (2018), we do not have access to a normative database of age-matched healthy control subjects. Therefore, we selected the ^{18}FDG PET scans of 45 age-matched control patients (19 females and 27

males; mean age 63.0 ± 9.1 years; 237.8 ± 52.4 MBq) from our institutional data base including 813 (as of May 2020) ^{18}FDG PET scans acquired under identical conditions with the aforementioned PET system, in whom somatic CNS diseases were carefully excluded, using a step-wise approach: (1) age 50 to 90 years (leaving n = 603, in whom n = 230 additional amyloid (Aβ) PET and dopamine transporter (DAT) SPECT studies were available); (2) normal cerebral ^{18}FDG PET according to clinical PET reports (including results of visual reads and statistical analyses using three-dimensional stereotactic surface projections; first independently, then consensually reviewed by two experienced nuclear medicine physicians, see Methods) and normal Aβ PET and/or DAT studies (if available; according to clinical reports; leaving n = 65); (3) no diagnosis of a somatic CNS disease by the referring physician during follow-up (along with exclusion of relevant structural brain lesions by CT or MRI in all patients, normal Aβ PET in n = 10 and normal DAT SPECT in n = 7; leaving n = 47); (4) no suspicious pattern of regional hyper- or hypometabolism on voxel-statistical analyses of each subject compared to all other subjects (methodology see Methods; SPM single-subjects *t* test with age as covariate and proportional scaling using the standard SPM standard procedure; voxel-level $p < 0.001$, cluster extent threshold $k > 30$ voxels; leaving n = 45).

5. Principal components analysis (PCA)

Each subject's three-dimensional image data were first converted to a continuous row vector and then embedded in a group data matrix. Each data entry was transformed to logarithmic form, and the data matrix was centered by each row's mean value. The deviation from both subject and group means represented the resulting subject residual profile image. PCA was applied to the covariance matrix to derive orthogonal eigenvectors and associated eigenvalues. The spatial eigenvectors were principal component (PC) image patterns given by the scaled subprofile model PCA. PCs related to the explored group difference were associated with the highest total variance accounted for by the eigenvector. To identify a significant pattern, different combinations of PC were tested on the basis of the following statistical criteria: the analysis was limited to the first set of contiguous PC that accounted for the top 50%

of the variability in the dataset, and the best combination of these PC was selected by a logistic regression analysis with group as the dependent variable and subject scores for the PC as the independent variable. The obtained pattern represented spatially covariant voxels associated with the group difference, with each voxel being specifically weighted toward its relative contribution.

6. Assessment of regional ^{18}FDG uptake

For exploratory analyses of the covariance patterns in terms of absolute regional glucose metabolism, we assessed mean ^{18}FDG uptake as a surrogate marker of the cerebral metabolic rate of glucose (CMR_{glc}) in the voxel with 10% highest weights, both for negative (relative hypometabolism) and positive (relative hypermetabolism) voxel weights.

Mean ^{18}FDG uptake (C_i^*) was expressed as standardized uptake value (*SUV*), accounting for decay-corrected injected ^{18}FDG dose (*D*) per lean body mass (*LBM*; given negligible uptake of ^{18}FDG in body fat) and plasma glucose level (C_p), which should be proportional to CMR_{glc} according to the simplified equation by Rhodes *et al.*, 1983:

$$CMR_{glc} = \frac{C_p}{LC} \times \frac{C_i^*(T)}{\int_0^T C_p^*(t)dt} \sim C_p \times \frac{C_i^*(T)}{D/LBM} = SUV,$$

with *LC* being a constant (so-called lumped constant) and assuming a linear relationship between the time integral of the plasma input function ($\int_0^T C_p^*(t)dt$) and *LBM*-normalized injected dose.

7. Neuropathological examination

First, the brain was fixed in 4% formalin for seven days. After sectioning the tissue, biopsies were taken for microscopic examination. The tissue was dehydrated in a tissue processing machine (Leica ASP300, Leica) for three days. After paraffin embedding, the tissue was cut into 3 µm thick sections and mounted onto Superfrost® objective slides (R. Langenbrinck). For initial deparaffinization, the slides were incubated at 80°C for one hour. The slides were then deparaffinized in Xylene and cooked in citrate buffer for 40 minutes (Target Retrieval Solution, DAKO, # S1699). The immunohistochemical reactions

for HLA-DR (1:400, DAKO, #M0775) and CD3 (1:50, Novocastra, #NCL-L-CD3-565) were performed using the EnVision™ FLEX system (DAKO, # K8000). The sections were counterstained with Gill's Haematoxylin (Merck Millipore, #1.05175.0500) and incubated in an ascending alcohol series, followed by incubation in Xylene. Xylene-based Vitro-Clud® (R. Langenbrinck, # 04-0001) was used as mounting reagent. Images were taken with 4x and 20x objectives (Leica, DFC450).

Supplementary Results

1. Allocation to diagnostic procedures

The Venn diagram of **Supplementary Figure 1** indicates the breakdown of allocation to ^{18}FDG PET, MRI and to the neuropsychological test battery (NPSY) as many patients received more than one investigation. With respect to CSF analysis (n = 4), two patients also received PET, MRI and NPSY, one patient also received MRI and NPSY and one patient only received PET. The reasons that diagnostic procedures were discarded are mentioned in **Figure 1**.

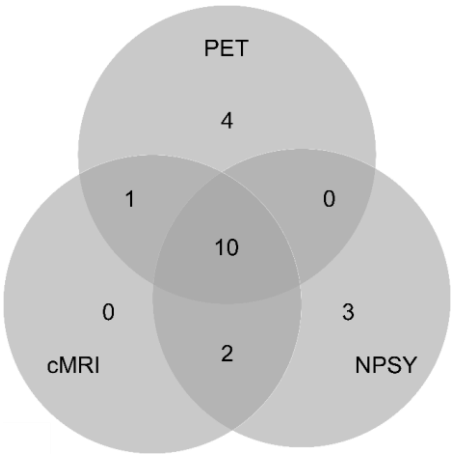

Supplementary Figure 1

There were no significant differences in age or MoCA score for patients examined with MRI (p = 0.29 for age; p = 0.57 for MoCA) or PET (p = 0.53 for age; p = 0.61 for MoCA) compared to the rest of the cohort. Patients examined with the neuropsychological battery had a similar MoCA performance (p = 0.23) but were slightly younger (p = 0.03) than the rest.

2. Neuropathological examination

Macroscopic findings:

The brain weighed 1280 g in a formalin-fixed state. Looking at the convexity of the cerebrum, symmetrically arranged hemispheres with a regular gyration and a moderate blood stasis could be seen. The leptomeninges were delicate and translucent. The bottom view of the brain showed regular anatomical conditions without signs of upper or lower incarceration. The Willis' circle was regular. There was a low grade arteriosclerosis of the vessels supplying the brain without significant lumen constriction. On a series of frontal sections through the cerebral hemispheres, the grey-brown cortical band and the white matter were well distinguishable and normal in color and consistency. The ventricular system was symmetrical and of age-appropriate width. The mammilary bodies, the hippocampus formation, the thalami and the basal ganglia were normally configured on both sides of the cerebral slices and could be easily delimited. Horizontal sections through the midbrain showed a regular pigmented substantia nigra and a delimitable nucleus ruber on both sides. The cerebral aqueduct was freely continuous. Further horizontal sections through the pons and the rostral part of the medulla oblongata as well as horizontal sections through the cerebellum did not show pathological findings macroscopically. The enclosed parts of the dura mater showed a reflecting inner side. At the cerebral falx, a tumorous growth was visible. For illustration see **Supplementary Figure 2**.

Microscopic findings:

Histologically, the tumorous growth at the cerebral falx was identified as a meningioma. Throughout the brain (frontal, temporal and occipital cortical tissue, hippocampus, basal ganglia, brain stem and cerebellum), no bleedings or necrotic areas were observed. Corpora amylacea were found in different regions. In the hippocampus, minor calcifications were present. Since H&E stainings indicated a gliosis, the tissue was further characterized by immunhistochemistry. In the immunohistochemical reaction for HLA-DR, a pronounced, bilateral microgliosis was observed in the white matter of the cerebellum,

reaching from the cerebellar vermis to the dentate nucleus. The HLA-DR-positive cells presented with an activated, spiky morphology. Furthermore, they regularly formed roundish cell conglomerates, so-called nodules. Similar changes were observed in the hippocampal formation and – to a lower extend – in the white matter of the frontal cortical tissue. In neighboring grey matter parts, the HLA-DR-positive cells retained a rather homeostatic morphology. Very few cells were detectable in the immunohistochemical reaction for CD3. Those cells appeared vessel-associated. In the absence of massive parenchymal T cells, no signs of neuroinflammation were observed. The virus detection of cerebellar FFPE tissue (rt-PCR) could not be evaluated for technical reasons.

Supplementary Figure 2: Bottom (**A**), aerial (**B**), righthand (**C**) and lefthand view (**D**) of the brain. **E**: an overview of coronal sections through the cerebrum, horizontal sections through the cerebellum and the enclosed parts of the dura mater. **F**: a series of horizontal sections through the brain stem. Exemplary sections of the cerebrum and the cerebellum from **E** are shown in **G** and **H**, respectively. A falx meningioma can be observed in **I**.

Supplementary Tables

Supplementary Table 1: Cognitive test battery

Test	Outcome variable	Domain
Hopkins Verbal Learning Test Revised (HVLT-R; Brandt and Benedict, 2001)	Score Total Learning (max 36)	Memory
	Score Delayed recall (max 12)	Memory
	Score Recognition (max 12)	Memory
Trail Making Test Part A (Lezak, 1995)	Time (s)	Attention
Trail Making Test Part B (Lezak, 1995)	Time (s)	Executive function
Stroop test Word reading (Bäumler, 1985)	Time (s)	Attention
Stroop test: Color naming (Bäumler, 1985)	Time (s)	Attention
Stroop test: Interference (Bäumler, 1985)	Time (s)	Executive function
Digit span (Lepach and Petermann, 2012)	Digits forward (no of correct trials)	Attention
	Digits backwards (no of correct trials)	Executive function
Symbol digits modalities test (SDMT; Langdon *et al.*, 2012)	Symbols / 90 s	Attention
Semantic Fluency (animals; Aebi *et al*., 2002)	Words / 60 s	Executive function
Phonemic Fluency (S- words; Aebi *et al*., 2002)	Words / 60 s	Executive function

Supplementary Table 2: Anamnestic data

	n of 29 patients (%)
Neuropsychology	
Temporary confusion	4 (14%)
Cognitive deficits	9 (31%)
Amnesic aphasia	2 (7%)
Hallucinations	1 (3%)
Cranial nerves	
Blurred vision	1 (3%)
Impairment of smell	22 (76%)
Cacosmia	7 (24%)
Headache	15 (52%)
Pain intensity on numerical rating scale (0 is minimum, 10 is maximum) mean (SD)	5.0 (1.8)
Diplopic images	1 (3%)
Worsening of a pre-existing facial nerve palsy	1 (3%)
Vertigo	6 (21%)
Impairment of gustation	22 (76%)
Sensorimotor function	
Dysarthria	1 (3%)
Fine motor impairment	2 (7%)
Whole body hyperalgesia	2 (7%)
Impairment/insecurity of gait	5 (17%)

Supplementary Table 3: Single item scores of the MoCA test

MoCA Item scores	**mean (SD)**
Trail Making (max. 1)	0.69 (0.46)
Cube copying (max. 1)	0.57 (0.49)
Clock drawing (max. 3)	1.92 (0.91)
Naming (max. 3)	2.81 (0.39)
Digit span (max. 2)	1.35 (0.55)
Letter A Tapping (max. 1)	0.81 (0.39)
Subtraction (max. 3)	2.42 (0.88)
Sentence repetition (max. 2)	1.73 (0.59)
Word Fluency (max. 1)	0.31 (0.46)
Abstraction (max. 2)	1.23 (0.89)
Delayed word recall (max. 5)	1.92 (1.70)
Orientation (max. 6)	5.61 (0.68)

Supplementary References

Aebi C, Monsch AU, Berres M, Brubacher D, Staehelin HB. Validation of the German CERAD-neuropsychological assessment battery. 2002

Bäumler, G. Farbe-Wort-Interferenztest (FWIT) nach J.R. Stroop. 1985

Brandt, J, Benedict, RHB. Hopkins verbal learning test – Revised. Administration manual. Lutz, FL: Psychological Assessment Resources. 2001

Egger K, Rau A, Yang S, Klöppel S, Abdulkadir A, Kellner E, et al. Automated voxel- and region-based analysis of gray matter and cerebrospinal fluid space in primary dementia disorders. Brain Res 2020; 1739: 146800.

Langdon DW, Amato MP, Boringa J, Brochet B, Foley F, Fredrikson S, et al. Recommendations for a Brief International Cognitive Assessment for Multiple Sclerosis (BICAMS). Mult Scler Houndmills Basingstoke Engl 2012; 18: 891–8.

Lazar RM, Pavol MA, Bormann T, Dwyer MG, Kraemer C, White R, et al. Neurocognition and Cerebral Lesion Burden in High-Risk Patients Before Undergoing Transcatheter Aortic Valve Replacement. JACC Cardiovasc Interv 2018; 11: 384–92.

Lepach, AC und Petermann, F. Wechsler Memory Scale Revised (WMS-R). 2012

Lezak MD. Neuropsychological assessment. 3rd ed. New York: Oxford University Press; 1995

Rhodes CG, Wise RJ, Gibbs JM, Frackowiak RS, Hatazawa J, Palmer AJ, et al. In vivo disturbance of the oxidative metabolism of glucose in human cerebral gliomas. Ann Neurol 1983; 14: 614–26.

Shattuck DW, Mirza M, Adisetiyo V, Hojatkashani C, Salamon G, Narr KL, et al. Construction of a 3D probabilistic atlas of human cortical structures. NeuroImage 2008; 39: 1064–80.

Shattuck DW, Mirza M, Adisetiyo V, Hojatkashani C, Salamon G, Narr KL, et al. Construction of a 3D probabilistic atlas of human cortical structures. NeuroImage 2008; 39: 1064–80.

Speck I, Arndt S, Thurow J, Blazhenets G, Aschendorff A, Meyer PT, et al. 18F-FDG PET Imaging of the Inferior Colliculus in Asymmetric Hearing Loss. J Nucl Med Off Publ Soc Nucl Med 2020; 61: 418–22.

Weiner MW, Aisen PS, Jack CR, Jagust WJ, Trojanowski JQ, Shaw L, et al. The Alzheimer's Disease Neuroimaging Initiative: Progress report and future plans. Alzheimers Dement 2010; 6: 202-211.e7.